

A Backpropagation Imaging Technique for Subsampled Synthetic Apertures

Yuri Álvarez López, Jaime Laviada, Ana Arboleya, and Fernando Las-Heras Andrés, *Senior Member, IEEE*

Abstract—Synthetic Aperture Radar (SAR)-based microwave imaging systems have been widely used in a great variety of application areas, ranging from Earth monitoring to nondestructive testing. The scanning speed is one of the key performance indicators of SAR-based imaging systems. One possibility to increase it is by widening the distance between measurements. However, this results in the presence of grating lobes which degrade the recovered microwave SAR images. To overcome this issue, this contribution presents a novel methodology that introduces the amplitude and phase of the field radiated by the transmitting and receiving antennas of the SAR system in the backpropagation imaging algorithm. The method takes advantage of the directive pattern of the Tx/Rx antennas to reduce the level of the grating lobes appearing in the SAR image. Results presented in this contribution confirm the effectiveness of the proposed methodology to work with subsampled apertures while minimizing the impact of the grating lobes in the SAR images. Subsampling rates of, at least, one wavelength, have been achieved while keeping the quality of the recovered SAR images similar to the ones retrieved when the Nyquist sampling rate is fulfilled.

Index Terms—Synthetic Aperture Radar (SAR), microwave imaging, backpropagation, grating lobes, subsampling.

I. INTRODUCTION

SYNTHETIC Aperture Radar (SAR) is a remote sensing technique that has been widely used in a variety of application areas, e.g. Earth observation [1], agriculture [2], topography [3], nondestructive testing applications [4], or landslides monitoring [5]. In SAR systems, the radar module is mounted on a moving platform (e.g., an airplane, a satellite or a robotic arm) so that radar samples are usually collected at a constant rate along the path followed by the platform. Then, these radar samples are coherently processed so that the resolution of the SAR system is equivalent to the one of a physical array having the same length as that of the SAR system path [6].

Conventional SAR processing requires the radar samples to fulfill the Nyquist sampling rate, which eventually limits either the spacing along the physical direction (if any) or the scanning speed along the virtual direction of the SAR system. In the case of monostatic or, equivalently, quasi-monostatic microwave imaging systems, like the ones studied in this contribution, the

theoretical sampling rate to avoid aliasing is $\lambda/4$, i.e. twice the sampling rate of bistatic systems [7]. However, in practice, a minimum sampling rate criterion of $\lambda/2$ is widely adopted provided the transmitting (Tx) and receiving (Rx) antennas are not omni-directional. Thus, a microwave SAR imaging system working in the 14-16 GHz frequency band would require a spatial sampling of 1 cm (according to the $\lambda/2$ sampling rate criterion considering the center frequency of 15 GHz) to fulfill the Nyquist sampling rate. If the radar module of this SAR system has a processing rate of 50 samples per second, then, the maximum speed at which the SAR system can be moved will be 50 cm/s.

A. An overview of the different strategies to increase the scanning speed in microwave SAR systems

There are several possibilities to increase the scanning speed of a SAR system:

i) *Use of a microwave/radar subsystem capable of faster transmission/processing rates.* This solution relies on enhanced hardware features (e.g., multiple Tx/Rx channels, or faster digital signal processing hardware and software), which could result in a more complex and, thus, more expensive SAR imaging system. Besides, some SAR imaging systems require the correlation of the microwave measurements with data provided by other sensors (e.g., pictures taken by a camera). In these cases, the acquisition speed is limited by the sensor with the slowest data rate.

ii) *Decreasing the spatial sampling rate, so that the spacing between two consecutive samples is widened.* The major drawback is the presence of grating lobes, whose spacing is inversely proportional to the sampling rate.

Increasing the spacing between samples is a strategy closely related to the design and implementation of phased array systems, where different techniques to reduce the number of elements of the array, while minimizing the impact of grating lobes, have been developed. Among them, it can be cited:

- *Use of two different arrays for transmission (Tx) and reception (Rx)* (Fig. 1 (b)), so that the grating lobes of the Point Spread Function (PSF) associated with each array cancel each other [8]-[10]. A similar concept, based on the multiplication of patterns with different grating lobes arrangements, is proposed in [11].

This work was supported in part by the Principado de Asturias / FICYT under grant “Ayudas para grupos de investigación de organismos del Principado de Asturias durante el período 2021-2023”, reference AYUD/2021/51706; and by the Ministerio de Ciencia e Innovación of Spain, Agencia Estatal de Investigación of Spain, and Fondo Europeo de Desarrollo Regional (FEDER) under projects PID2021-122697OB-I00 (“META-IMAGER”) and TED2021-131975A-I00 (“ANTHEM5G”).

Corresponding author: Y. Álvarez López.

Y. Álvarez López, J. Laviada, and F. Las-Heras Andrés are with the Department of Electrical, Electronics, Communications and Systems of the University of Oviedo. Edificio Polivalente, Mod. 8, Campus Universitario de Gijón. 33203, Asturias, Spain. Email: {alvarezuri, laviadajaime, flasheras}@uniovi.es.

A. Arboleya is with the Departamento de Teoría de la Señal y las Comunicaciones y Sistemas Telemáticos y Computación, Universidad Rey Juan Carlos. Fuenlabrada. 28943 Madrid, Spain. Email: ana.arboleya@urjc.es.

TIM-22-04874R1

- Use of a tapered feeding of the elements [12]. This includes well-known array synthesis techniques like Dolph-Chebyshev or Taylor [13].
- Use of sparse, nonregular distribution of the array elements, as illustrated in Fig. 1 (c). These sparse distributions are employed in Compressed Sensing (CS) imaging algorithms [14]-[16].

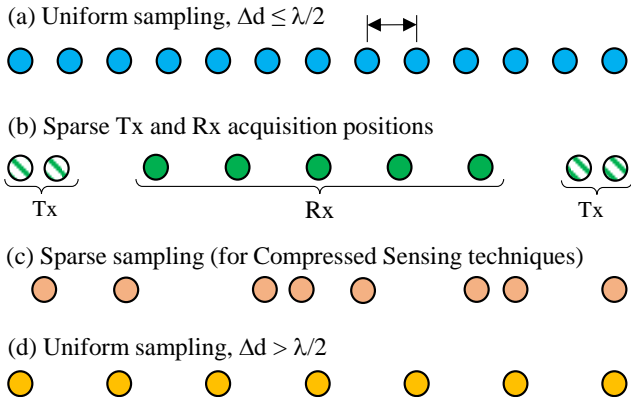


Fig. 1. Different schemes for synthetic aperture sampling. The one to be analyzed in this contribution is the last one (d).

Sampling schemes illustrated in Fig. 1 (b) and (c) are capable of reducing the number of required elements in the antenna array by more than 50% with respect to uniform distribution with $\lambda/2$ spacing between elements.

In SAR imaging systems, however, samples are usually acquired at a constant rate, with the SAR system mounted on a platform or vehicle that moves at a quasi-constant speed. In consequence, the implementation of uneven sampling schemes like the ones plotted in Fig. 1 (b) and (c) is not feasible. It would require the radar module to use a variable Tx/Rx rate and/or the variation of the scanning speed of the platform where the imaging system is mounted.

Another possibility to increase the spacing between samples in SAR systems is the combination of the synthetic aperture with a physical antenna array, similar to the subarray method presented in [11]. However, this would be redundant, as the idea of the synthetic aperture is to take advantage of the movement of the SAR imaging system to avoid the need for an antenna array. In addition, the size and weight of the antenna array are also limiting factors concerning the design and implementation of the SAR system.

Taking into account the aforementioned requirements and limitations for SAR systems, the sampling scheme depicted in Fig. 1 (d) would enable increasing the scanning speed of the SAR system. In this scheme, samples are evenly spaced, being the spacing greater than the Nyquist sampling rate (that is, greater than $\lambda/2$). This sampling scheme results in the presence of grating lobes that have an impact on the recovered SAR images. Consequently, the imaging algorithms used in subsampled synthetic apertures are challenged by the capability of providing SAR images as accurately as when the Nyquist sampling rate is fulfilled.

B. SAR imaging techniques

SAR processing algorithms provide a 2D or 3D reflectivity map of the imaged scenario from the scattered field measurements acquired along the observation domain (i.e., the path followed by the vehicle where the SAR system is mounted). This calculation of the reflectivity can be also understood as a spectrum estimation problem.

One of the advantages of SAR imaging techniques is that no *a-priori* information about the shape, size, or position of the targets is required. The only consideration to be taken into account is that the size of the investigation or imaging domain must be set large enough to ensure that the targets to be imaged are contained within it. Conversely, inverse scattering methods based on model-based techniques [17] need an initial guess of the target or targets-under-test.

Different methods have been developed to retrieve the reflectivity image from the scattered field measurements [18],[19]:

- *Fourier-based imaging techniques* are the most efficient imaging algorithms in terms of computational efficiency [20],[21]. These techniques require the observation and imaging domains to be uniformly sampled, otherwise requiring an interpolation step of the measurements onto a regular grid [22].

- *Backpropagation algorithms* are less efficient than Fourier-based ones in terms of computational complexity, but they are able to work with acquisition domains that are not uniformly sampled [23]. One of these backpropagation algorithms is Delay-and-Sum (DAS) [24]. This method has been widely used not only in microwave imaging applications but also in seismics and acoustics [25].

- *Full-wave equation methods, and tomographic approaches.* They can model accurately the imaged scenario. Besides, they can retrieve the constitutive parameters of the targets [26]-[28]. The main issue is their high computational complexity, which limits their applicability to electrically large scenarios.

- *Compressed sensing techniques.* These methods can deal with subsampled, sparse apertures (see Fig. 1 (c)). However, they also exhibit a moderate computational cost, thus limiting the applicability. Moreover, the problem must be sparse (after a linear transformation), which is also a strong requirement. Besides, as stated in Section I.A, the use of irregular sampling patterns is not suitable for SAR systems mounted on vehicles or platforms moving at a constant speed, with radar modules working at a uniform data acquisition rate [14]-[16],[29].

C. SAR imaging techniques for subsampled apertures

A comparison of several backpropagation imaging methods is presented in Table I, discussing their main features and limitations, as well as the feasibility to handle subsampled apertures where the samples are evenly spaced (see Fig. 1 (d)). For example, in the methodology presented in [30], up to 2λ subsampling was achieved for a multistatic configuration (which can be considered 1λ in an equivalent monostatic arrangement). And in [31], the spacing between elements for a phased antenna array was 1λ .

In [32], the authors presented a modified DAS algorithm where the phase of the field radiated by the Tx/Rx antennas was considered. It was proved that proper characterization of the

TIM-22-04874R1

phase of the field radiated by the Tx/Rx antennas resulted in better imaging of the targets, especially when placed in the near-field (NF) region of the Tx/Rx antennas. Besides, if the phase of the radiated field is accurately characterized, the targets are imaged at the right range position, avoiding the need for additional calibration to correct the offset between the true position of the targets and the position where the targets are imaged. However, the method described in [32] lacked the capability to work with subsampled apertures. This limitation is common to those imaging algorithms that only consider the phase term in the backpropagation of the field scattered by the targets.

TABLE I
COMPARISON OF BACKPROPAGATION IMAGING METHODS

Reference	Main features	Advantages	Limitations / disadvantages
[8]-[10], [22]	Fourier-based backpropagation imaging.	Very efficient from a computational point-of-view. Can deal with subsampled apertures, or arrays whose elements are spaced more than $\lambda/2$	Requires the combination of different sampling patterns for the Tx and for the Rx (not suitable for uniformly sampled apertures). Nonideal phase radiation pattern is not corrected.
[30]	Replication of the spectrum to image targets off-centered with respect to the aperture.	Capable of dealing with subsampled apertures (up to 2λ , multistatic architectures) Based on Fourier-based imaging (computationally efficient).	<i>A-priori</i> knowledge of the approximate size of the targets is required. Nonideal phase radiation pattern is not corrected.
[31]	Physical array with elements spaced 1λ	Supports subsampling, up to 1λ	Physical antenna array, which requires accurate calibration/equalization of the channels. Nonideal phase radiation pattern is not corrected.
[32]	Accurate characterization of the phase of the field radiated by the Tx/Rx antennas.	Targets are imaged at the right position without requiring a-priori calibration.	Requires the characterization of the Tx/Rx antennas of the imaging system. The field in the imaging domain needs to be calculated, increasing calculation time (but only once). Cannot deal with subsampled apertures.
[35], [36]	Patch modeling of the targets to suppress grating lobes.	Capable of dealing with subsampled apertures.	It requires the modeling of the targets. Nonideal phase radiation pattern is not corrected.
This contribution	Accurate characterization of both the amplitude and the phase of the field radiated by the Tx/Rx antennas.	Same as [32], plus capable of dealing with subsampled apertures (up to, at least, 1.08λ)	Requires the characterization of the Tx/Rx antennas of the imaging system. The field in the imaging domain needs to be calculated, increasing calculation time (but only once).

D. Aim and scope of this contribution

In this contribution, a novel backpropagation imaging method capable of overcoming the limitations of other imaging techniques to work with subsampled apertures is presented. This method is based on a modified version of the DAS algorithm [32], which has been extended by adding the amplitude of the field radiated by the Tx/Rx antennas. The proposed method shows that the addition of the amplitude term effectively reduces the level of the grating lobes in the SAR images even when the subsampling rate is greater than 1λ .

The novelties and limitations of the proposed methodology are summarized in the last row of Table I. The main advantages with respect to other imaging methods for subsampled apertures are: i) a-priori knowledge or modeling of the geometry of the targets is not required. ii) it is based on exploiting the directional properties of the Tx/Rx antennas of the SAR imaging system, so no additional hardware is required. This is of particular interest as this method can be used in a wide variety of SAR imaging architectures where the sampling scheme follows the pattern depicted in Fig. 1 (d). Besides, this method also inherits the advantages of the modified DAS algorithm of [32].

This manuscript is organized as follows: a review of the DAS algorithm is presented in Section II together with the proposed modification of the DAS to work with subsampled apertures. Section III analyzes the performance of the method when applied to subsampled apertures; for this purpose, two-dimensional (2D) simulation-based examples are considered. Next, experimental validation with two different measurement setups is presented in Section IV, where results obtained with the DAS algorithm, the modified DAS of [32], and the method described in this contribution are compared. Section IV also analyzes the impact of the accuracy of the Tx/Rx antenna characterization in the recovered SAR images. Finally, conclusions are drawn in Section V.

II. METHODOLOGY

A. An overview of the DAS imaging method

A basic scheme of a monostatic imaging system is depicted in Fig. 2. The transmitting (Tx) and receiving (Rx) antennas are displaced along the synthetic aperture (observation domain), whose length is L_{obs} . This aperture is discretized into N points, so the sampling rate is given by $\Delta L_{\text{obs}} = L_{\text{obs}}/(N-1)$. The center of the imaging domain is located at a distance R from the observation domain and has a cross-range or lateral size of L_{img} . The imaging domain is the area (2D) or volume (3D) that contains the target or targets to be imaged. As stated in Section I.B, no a-priori information about the number of targets and their location within the imaging domain is required.

The DAS backpropagation technique is described next: given the field scattered by the targets, E_{scatt} , acquired in the N positions of the synthetic aperture and in a frequency band discretized into N_f frequencies, the reflectivity in a point belonging to the imaging domain, $\rho(\vec{r}')$, is calculated as defined in (1) (further details can be found in Section 2.6 of [33]):

TIM-22-04874R1

$$\rho(\vec{r}') = \sum_{m=1}^{N_f} \sum_{n=1}^N E_{scat}(f_m, \vec{r}_n) e^{jk_0(f_m)(R_{Tx}(\vec{r}_n, \vec{r}') + R_{Rx}(\vec{r}_n + \vec{d}, \vec{r}'))} \quad (1)$$

where $R_{Tx}(\vec{r}_n, \vec{r}')$ and $R_{Rx}(\vec{r}_n + \vec{d}, \vec{r}')$ correspond to the Euclidean distance between the position of the Tx and Rx antennas at the n -th observation position (\vec{r}_n) and the imaging position \vec{r}' within the imaging domain. \vec{d} denotes the position vector between the Tx antenna and the Rx antenna. k_0 is the wavenumber at the m -th frequency, $k_0(f_m) = 2\pi f_m/c$.

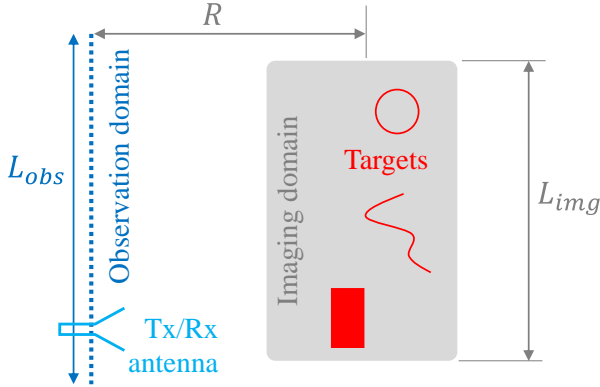


Fig. 2. Scheme of an imaging system (based on the configuration described in [35],[36]).

In the case of a monostatic configuration $\vec{d} = 0$ and $R_{Tx}(\vec{r}_n, \vec{r}') = R_{Rx}(\vec{r}_n, \vec{r}')$; that is, the transmitting (Tx) and receiving (Rx) antennas are located at the same position, $\vec{r}_{obs,n}$.

Similarly to other imaging techniques, the DAS algorithm is based on a far-field approach, that is, the backpropagation term corresponds to the phase term of a spherical wave. In some scenarios (e.g., when the targets are located within the near-field region of the Tx/Rx antennas), the effect of the antenna radiation pattern of the Tx/Rx antennas in the microwave imaging results is not negligible, as illustrated in [32] and in [34]. Furthermore, the phase difference between the spherical wave approach and the complex radiation pattern of the Tx and Rx antennas requires a calibration stage to compensate for the shifting in the position of the imaged objects.

To overcome the error due to the far-field approach, a modification of the DAS algorithm was proposed in [32]. It consisted of replacing the spherical wave phase term by the phase of the field radiated by the Tx/Rx antennas of the imaging system (2):

$$\rho(\vec{r}') = \sum_{m=1}^{N_f} \sum_{n=1}^N \left\{ E_{scat}(f_m, \vec{r}_n) \cdot e^{j((E_{rad,Tx}(f_m, \vec{r}_n, \vec{r}')^*) + (E_{rad,Rx}(f_m, \vec{r}_n, \vec{r}' + \vec{d})^*))} \right\} \quad (2)$$

where $\langle E_{rad,Tx}(f_m, \vec{r}_n, \vec{r}')^* \rangle$ and $\langle E_{rad,Rx}(f_m, \vec{r}_n, \vec{r}' + \vec{d})^* \rangle$ are the phase of the field radiated by the Tx and Rx antennas, respectively. Note that this formulation is valid for either monostatic or multistatic configurations.

B. Characterization of the grating lobes in subsampled apertures

As mentioned in Section I, one of the main challenges of SAR imaging systems is to increase the scanning speed without worsening the imaging capabilities. Widening the spacing between consecutive observation points beyond the Nyquist sampling rate (that is, $\Delta L_{obs} > \lambda/2$) results in the presence of grating lobes in the Point Spread Function (PSF), i.e., the image corresponding to a point-like target [35],[36]. Consequently, depending on the subsampling rate, the size of the imaging domain, and the distance between the imaging domain and the observation domain, replicas of the imaged targets may appear within the imaging domain [37],[30]. In other words, a subsampled observation domain results in aliasing in the spectral domain [38].

Sometimes it is possible to apply filtering techniques in the imaging (spatial) domain or in the spectral domain to remove the aliasing, as illustrated in [37],[30]. Another solution to mitigate the impact of aliasing in the SAR images, based on what is called a patch modeling of the targets, is presented in [35],[36].

For a monostatic imaging system, the condition that gives the minimum number of observation points N required to avoid the presence of grating lobes within the imaging domain is derived in [35],[36] (1):

$$N \geq \frac{2L_{obs}L_{img}}{R\lambda} + 1, \quad (3)$$

where λ is the wavelength at the center frequency (f_c) of the working frequency band, and R is the distance between the observation domain and the center of the imaging domain (see Fig. 2).

From (3), and for a subsampled array, it is possible to estimate the position where the grating lobes (and thus the replicas of the imaged targets) will appear in the imaging domain, d_{GL} :

$$d_{GL} = \frac{\lambda R}{2 \Delta L_{obs}} \quad (4)$$

A synthetic aperture can be studied as a virtual array. Consequently, the field radiated by the aggregation of all the positions within the synthetic aperture ($\vec{E}_{rad}(f, \vec{r})$) is the array factor of the virtual array ($AF(f, \vec{r})$) times the radiation pattern of the Tx/Rx antenna used in the SAR sensor ($\vec{E}_{rad,ant}(f, \vec{r})$):

$$\vec{E}_{rad}(f, \vec{r}) = \vec{E}_{rad,ant}(f, \vec{r}) \cdot AF(f, \vec{r}), \quad (5)$$

In the case of a linear array of N equally spaced elements (placed along the z -axis without loss of generality), the radiation pattern is given by:

$$\vec{E}_{rad}(f, \theta) = (\vec{E}_{rad,ant}(f, \theta)) \sum_{n=0}^{N-1} e^{jk_0(f)(n\Delta d)\cos(\theta)} \quad (6)$$

where Δd is the spacing between consecutive elements.

TIM-22-04874R1

Discarding coupling effects between the elements, this would be equivalent to the radiation pattern of a synthetic aperture where the SAR sensor follows a linear path (in the case of (6), the path would be in the z -axis).

In a particular case where the elements of the linear array are electrically small dipole-like antennas (or, equivalently, if the SAR sensor antenna is a dipole), the radiation pattern is given by (7):

$$\vec{E}_{rad}(f, \theta) = (\cos(\theta)\hat{\theta}) \sum_{n=0}^{N-1} e^{jk_0(f)(n\Delta d)\cos(\theta)} \quad (7)$$

In the case of subsampled apertures, if the radiation pattern of the element has certain directivity, then, the amplitude of the grating lobes is modified according to the shape of its radiation pattern, as illustrated in Fig. 3 (b). Conversely, when punctual, isotropic elements are considered, the grating lobes exhibit the same amplitude as the main lobe (Fig. 3 (a)). Thus, the use of directive antennas in physical or synthetic arrays would mitigate the effect of the grating lobes and, consequently, the aliasing in the imaging domain. An application example based on this concept was presented in [31], where the elements of the antenna array were spaced 1λ without degrading the beamsteering capabilities due to the grating lobes.

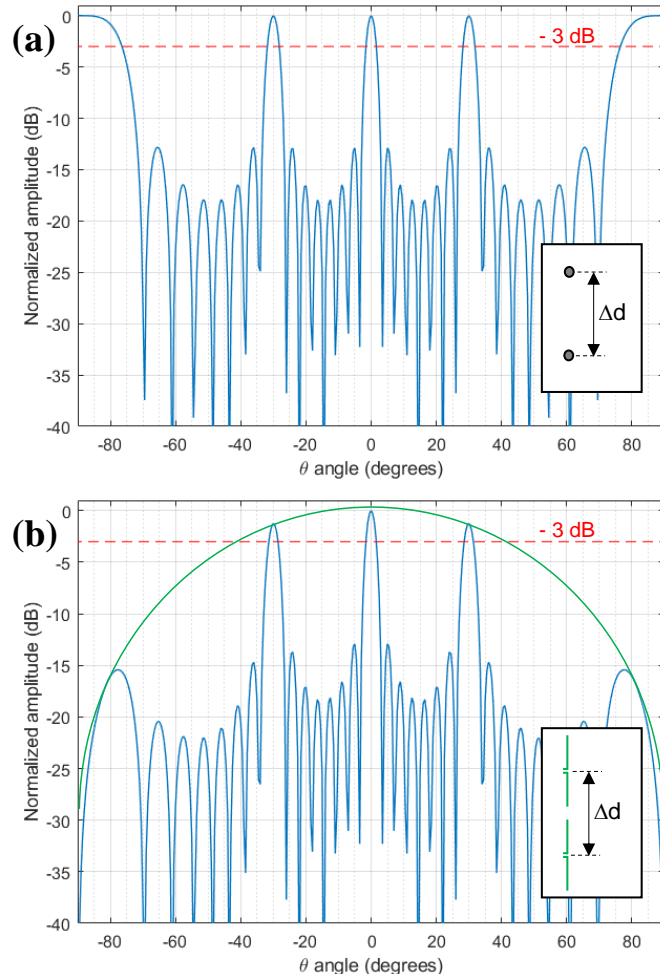


Fig. 3. Representation of the radiation pattern of an $N = 16$ -element antenna where the elements are placed along the z -axis and spaced Δd

$= 2 \lambda$. (a) Punctual, isotropic elements. (b) Dipole-like elements (the solid green line is the radiation pattern of the element).

C. Modification of the DAS imaging method to work with the amplitude and phase of the Tx/Rx antennas

In Section II.B it has been shown that, if the antenna used in a phased-array imaging system or in a SAR imaging system has certain directivity, then, the grating lobes will be attenuated. This minimizes the impact of the aliasing in the imaging domain. Thus, to take advantage of this feature, the imaging algorithm must be capable to take into account the radiation pattern of the Tx/Rx antenna.

One possibility is to model the synthetic aperture as a physical array, then using a full-wave method to calculate the field radiated by this physical array in the imaging domain, as well as its interaction with the targets. Next, a cost function relating the measured scattered field and the scattered field calculated with the full-wave model is minimized, where the unknowns in the full-wave model are usually the geometry and composition of the targets in the imaging domain [26] or a contrast function [27]. Full-wave model techniques require an initial guess of the shape and composition of the targets. Thus, depending on how close to the final solution this first guess is, the cost function to be minimized might converge or not. Besides, these inverse scattering techniques based on full-wave methods have a computational cost higher than Fourier-based or backpropagation imaging algorithms.

A simpler approach is proposed in this contribution. It is based on the modified DAS algorithm presented in [32], extending it to consider not only the phase of the field radiated by the Tx/Rx antenna but also the amplitude of the field as shown in (8). This formulation is valid regardless the placement of the targets with respect to the Tx/Rx antennas, that is, they can be located either in the near-field region of the antennas, or in the far-field region.

$$\rho(\vec{r}') = \sum_{m=1}^{M_f} \sum_{n=1}^N \left\{ \begin{array}{l} E_{scat}(f_m, \vec{r}_n) (E_{rad,Tx}(f_m, \vec{r}_n, \vec{r}'))^* \cdot \\ (E_{rad,Rx}(f_m, \vec{r}_n + \vec{d}, \vec{r}'))^* \end{array} \right\} \quad (8)$$

The flowchart of the methodology proposed in this contribution is summarized in Fig. 4. The first step is the characterization of the field radiated by the Tx/Rx antennas of the imaging system. For aperture-like antennas (e.g., horn antennas, Open-Ended Waveguide Antennas (OEWG)) it just requires the calculation of the fields on the aperture plane of the antennas, $E_{ap}(f_m, \vec{r}_{ap})$. Depending on the kind of antennas used in the SAR imaging system, several methods can be considered. In the case of OEWG and horn antennas, analytical models provide an accurate estimation of these aperture fields. For another kind of antenna, where these analytical models that predict the radiated fields might not be accurate enough, the use of an electromagnetic model of the antenna, derived from simulations or from the measurement of the field radiated by the antenna, will be required.

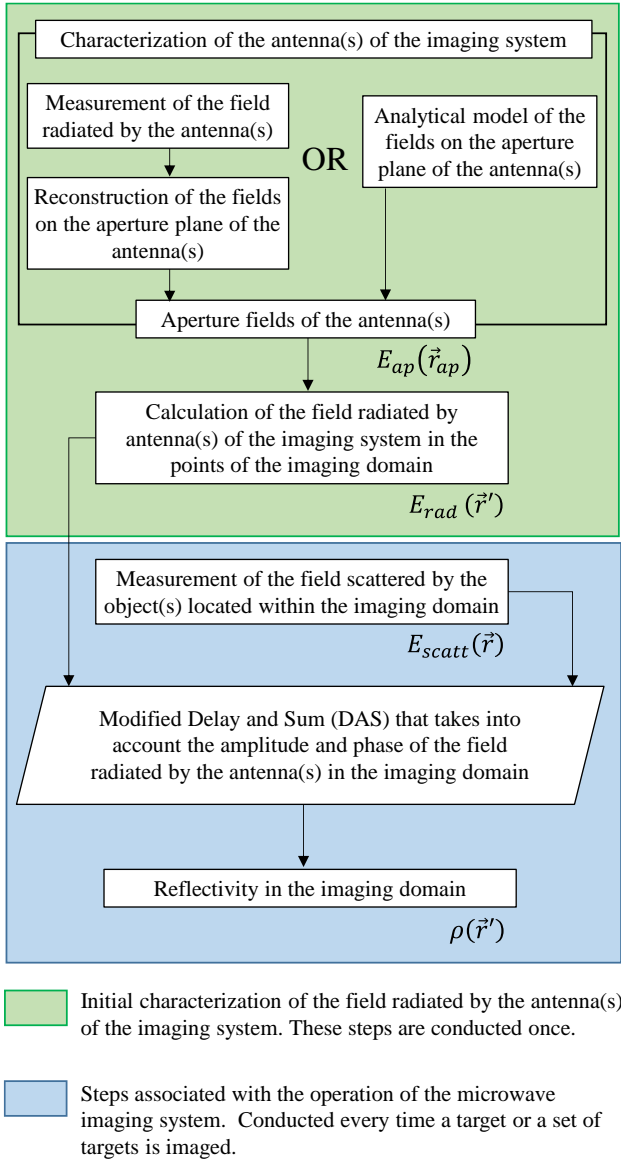


Fig. 4. Flowchart of the modified DAS algorithm that uses the field radiated by the antenna(s) of the imaging system.

Next, the aperture fields of the Tx/Rx antennas are used to calculate the field radiated by these antennas within the investigation or imaging domain, $E_{rad}(f_m, \vec{r}_n, \vec{r}')$ (the formulation is described in Annex I). As stated in [32], this procedure has to be conducted for every position \vec{r}_n of the observation domain. This step has to be conducted once (e.g., once the microwave imaging setup has been implemented and commissioned). It must be stressed that $E_{rad}(f_m, \vec{r}_n, \vec{r}')$ models the propagation of the field radiated by the Tx/Rx antennas. Consequently, it does *not* depend on the targets placed in the imaging domain.

Once the field radiated by the Tx/Rx antennas has been calculated in the imaging domain, the system is ready to perform measurements. This, the targets can be placed in the microwave imaging system to measure the scattered field, $E_{scat}(f_m, \vec{r}_n)$. Finally, (8) is applied to recover the reflectivity in the imaging domain, $\rho(\vec{r}')$.

III. SIMULATION-BASED ASSESSMENT OF THE PROPOSED METHODOLOGY

In this section, the methodology presented in Section II to coarsen the sampling requirements of the synthetic aperture while minimizing the effect of grating lobes in the imaging domain is analyzed by means of simulation-based examples.

A. Single scatterer

First, a single circular metallic scatterer is considered as a target-under-test. The simulated two-dimensional (2D) monostatic imaging system uses a 3 cm wide OEWG working in the 12 GHz to 14 GHz band as the Tx/Rx antenna. This OEWG is moved along a $L_{obs} = 10$ cm linear observation domain (i.e., the synthetic aperture). The distance between the observation domain and the circular target is $R = 75$ cm. The observation domain is sampled every $\Delta L_{obs} = 1$ cm (0.43λ at 13 GHz) to fulfill the Nyquist sampling rate.

Imaging results are depicted in the first row of Fig. 5. In Fig. 5 (a) the target is imaged by using the DAS backpropagation algorithm (1) that considers a far-field approach of the phase term, that is, $e^{-jk_0 R}$. This far-field approach does not take into account the additional phaseshift that can be introduced by the actual field radiated by Tx/Rx antennas. Conversely, both the modified DAS algorithm (2) presented in [32] and the version presented in this contribution (8) take into account the phase of the actual field radiated by the OEWG antenna. In consequence, when these algorithms are applied, the target is imaged at the right position ($R = 75$ cm), as observed in Fig. 5 (b) and (c), because the phase of the field is accurately modeled.

Concerning shape and aspect ratio of the imaged target, there are no significant differences between the three imaging methods tested (DAS with the far field approach, modified DAS considering only the phase of the field radiated by the OEWG, and modified DAS considering the complex field radiated by the OEWG).

Next, the imaging system is assessed again for a sampling rate of $\Delta L_{obs} = 2.5$ cm (1.08λ at 13 GHz). As observed in Fig. 5 (d) and (e), replicas of the target appear in the imaging domain. These replicas are approximately at 30 cm from the position of the target, which is in agreement with the distance predicted by (4) [35],[36]:

$$d_{GL} = \frac{\lambda R}{2 \Delta L_{obs}} = \frac{2.3 \text{ cm} \times 75 \text{ cm}}{2 \times 2.5 \text{ cm}} = 34.5 \text{ cm} \quad (9)$$

In Fig. 5 (f), the modified DAS that makes use of the complex field radiated by the OEWG in the imaging domain is applied. In this case, the replicas of the target are not observed as they are attenuated by the radiation pattern of the OEWG.

To confirm this result, the sampling rate is further decreased to $\Delta L_{obs} = 5$ cm (2.16λ at 13 GHz). The recovered reflectivity is plotted in Fig. 5 (g)-(i) for the compared imaging algorithms. The replicas of the target appear every 15 cm, in agreement with the theoretical value obtained with (4) (17 cm). In Fig. 5 (i), only the replicas closest to the true position of the target appear in the imaging domain. The reason is that the radiation pattern

TIM-22-04874R1

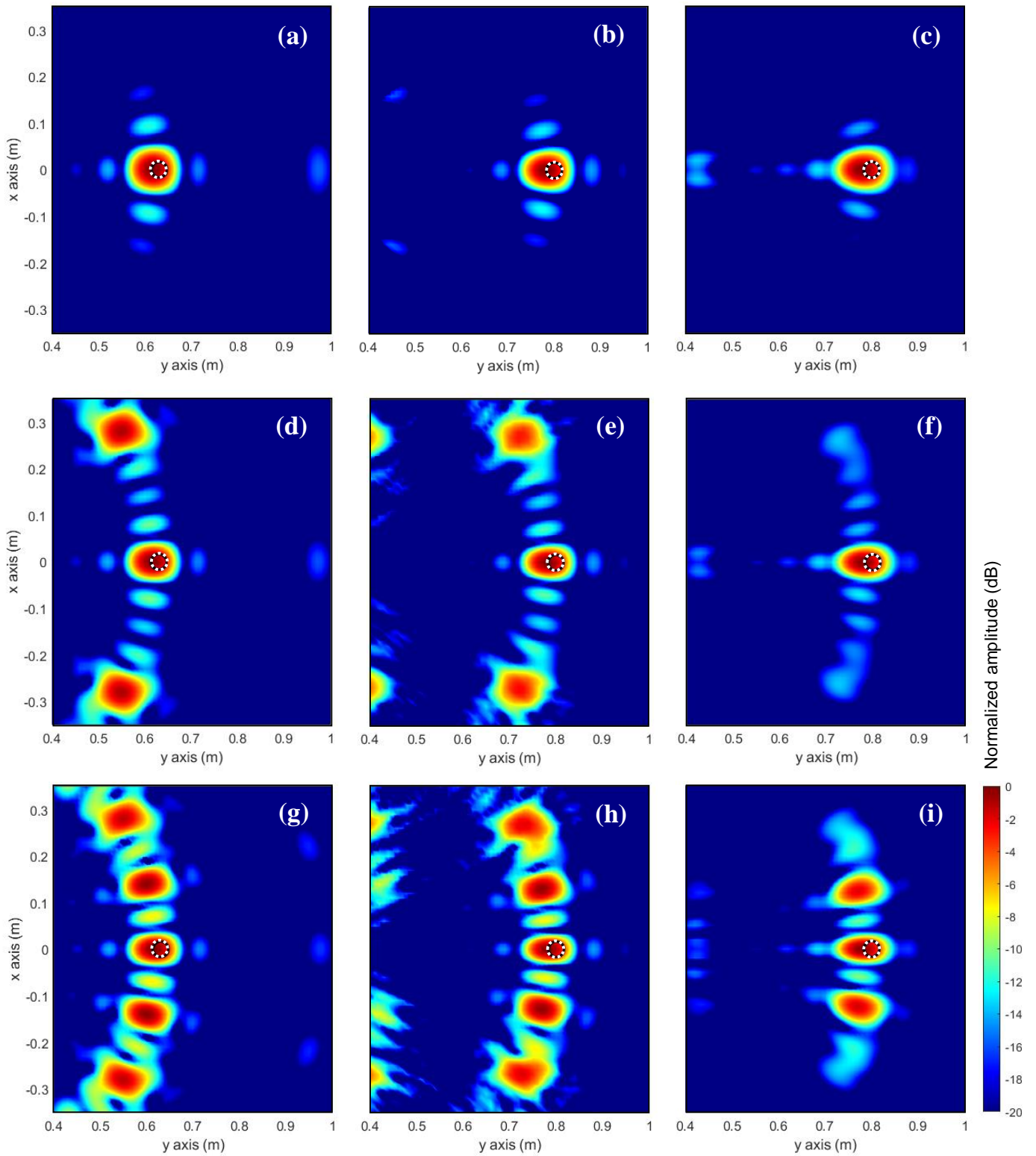


Fig. 5. Imaging results of a circular metallic scatterer when the Tx/Rx antenna is an OEWG. (a)-(c) $\Delta L_{obs} = 0.43 \lambda$, (d)-(f) $\Delta L_{obs} = 1.08 \lambda$, (g)-(i) $\Delta L_{obs} = 2.16 \lambda$. Left column: reflectivity calculated using the far field approach. Center column: reflectivity calculated using the phase of the field radiated by the OEWG. Right column: reflectivity calculated using the complex field radiated by the OEWG. The black and white line represents the position and geometry of the target (in the case of the far field approach, left column, the target is plotted shifted with respect to its true position).

TIM-22-04874R1

of the OEWG is not directive enough to attenuate the grating lobes associated with these replicas.

The influence of the radiation pattern of the Tx/Rx antenna of the monostatic imaging system is analyzed in the results presented in Fig. 6. The left row of Fig. 6 corresponds to the results when the Tx/Rx antenna is an OEWG, whereas the right row shows the imaged circular target when a more directive antenna (a horn antenna whose aperture width is 11 cm) is considered. No significant differences are observed between the conventional DAS with the far-field approach (Fig. 6 (a) and (b)) and the modified DAS that uses the phase of the Tx/Rx antenna (Fig. 6 (c) and (d)).

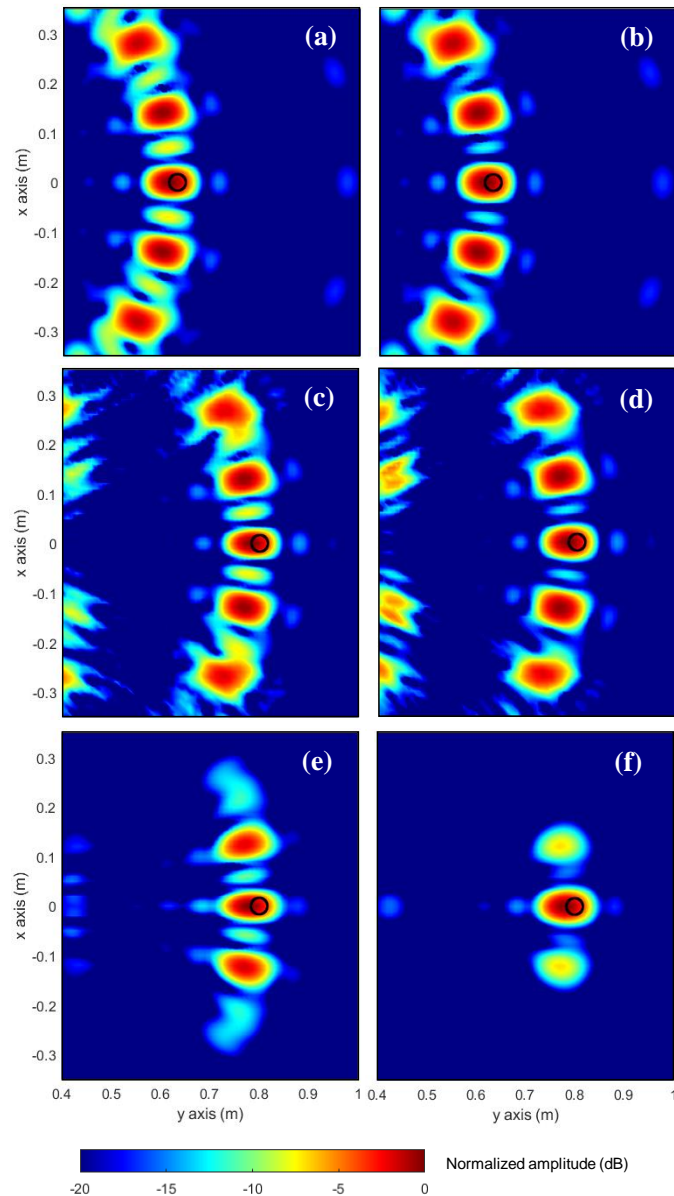


Fig. 6. Imaging results of a circular metallic scatterer, with $\Delta L_{obs} = 2.16 \lambda$. (a),(c),(e) The Tx/Rx antenna is an OEWG. (b),(d),(f) The Tx/Rx antenna is a horn antenna. (a),(b) Reflectivity calculated using the far field approach. (c),(d) Reflectivity calculated using the phase of the field radiated by the Tx/Rx antenna (e),(f) Reflectivity calculated using the complex field radiated by the Tx/Rx antenna.

However, when the amplitude of the Tx/Rx antenna is introduced in the imaging method (Fig. 6 (e) and (f)), the impact in the mitigation of the replicas of the target is noticed. The horn antenna is more directive than the OEWG and, consequently, the replicas are more attenuated in Fig. 6 (f) than in Fig. 6 (e). For the sake of clarity, Fig. 7 shows an overlay of the field radiated by the antenna of the monostatic imaging system and the reflectivity recovered in Fig. 6 (e) and (f), that is, when the observation domain is subsampled ($\Delta L_{obs} = 2.2 \lambda$). It is noticed the correlation between the amplitude of the radiation pattern of the Tx/Rx antenna and the amplitude of the replicas of the imaged target.

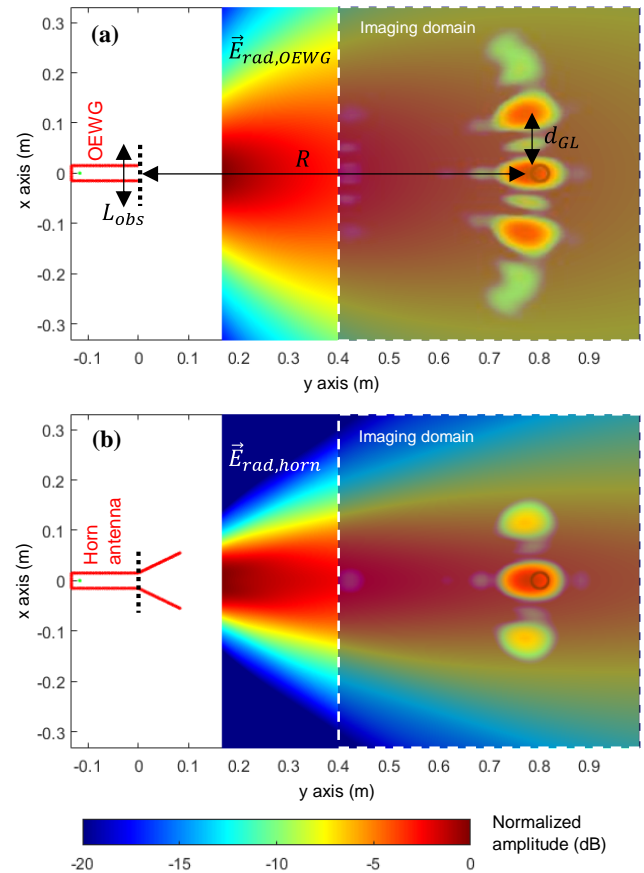


Fig. 7. Scheme of the monostatic imaging scenario, where the reflectivity in the imaging domain is plotted on top of the field radiated by the antenna. (a) OEWG. (b) Horn antenna.

B. Electrically large scatterers

This section analyzes the impact of the grating lobes of subsampled apertures when electrically large scatterers are imaged. This is the case of airborne SAR systems devoted to obtaining SAR images of targets placed on or over the ground [39],[40]. With respect to the scenario presented in Section III.A, the working frequency band has been broadened to 3 GHz (12-15 GHz band), and the aperture has been widened to $L_{obs} = 55$ cm (from $y = -20$ cm to $y = 35$ cm). Both the OEWG and the horn antenna will be considered as Tx/Rx antennas for comparison purposes. Two targets have been considered: the same circular metallic scatterer of the previous section, at $y =$

TIM-22-04874R1

75 cm; and a flat metallic surface located at $y = 80$ cm that ranges from $x = -40$ cm to $x = +40$ cm (as observed in Fig. 8, the length of this surface exceeds the size of the imaging domain).

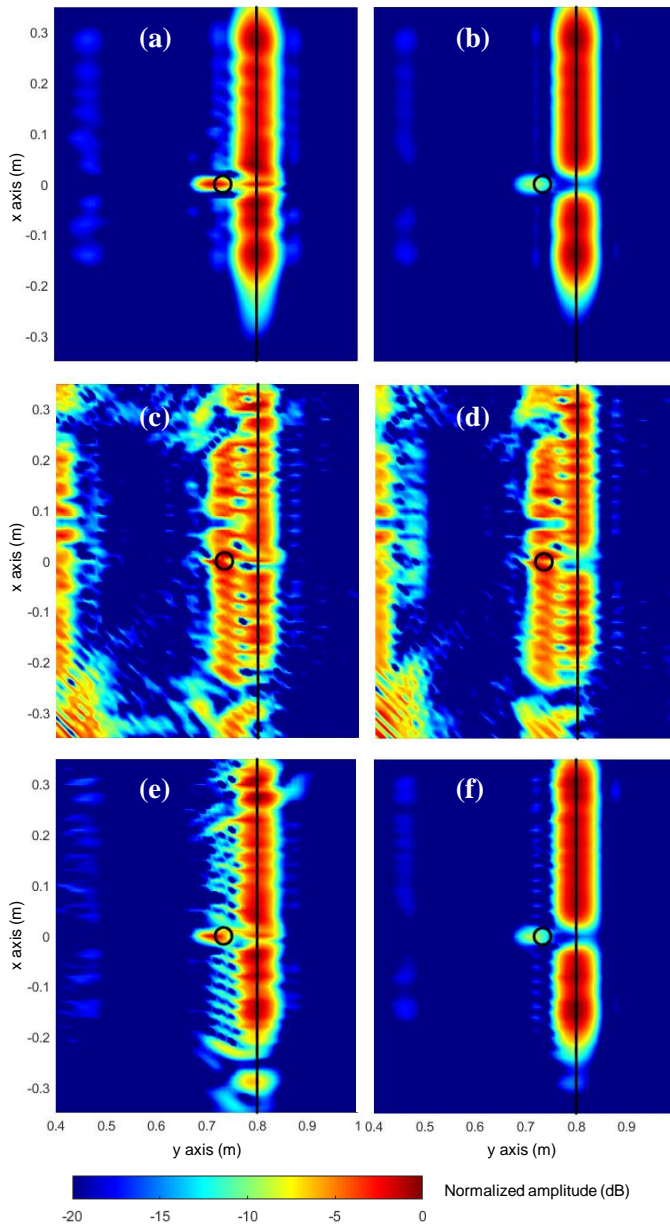


Fig. 8. Imaging results of a circular metallic scatterer placed in front of a metallic plate. Left column: the Tx/Rx is an OEWG. Right column: the Tx/Rx is a horn antenna. (a),(b) $\Delta L_{obs} = 1$ cm (0.45λ), reflectivity calculated using the phase of the field radiated by the Tx/Rx antenna. (c),(d) $\Delta L_{obs} = 2.5$ cm (1.13λ), reflectivity calculated using the phase of the field radiated by the Tx/Rx antenna. (e),(f) $\Delta L_{obs} = 2.5$ cm (1.13λ), reflectivity calculated using the complex field radiated by the Tx/Rx antenna.

In the results depicted in Fig. 8 (a) and (b), the observation domain is sampled every $\Delta L_{obs} = 1$ cm (0.45λ at 13.5 GHz), and the imaging algorithm is the modified DAS that makes use of the phase of the field of the Tx/Rx antenna. The circular metallic target placed in front of the metallic surface is imaged

with both the OEWG (Fig. 8 (a)) and the horn antenna (Fig. 8 (b)).

In Fig. 8 (c)-(f), the sampling rate is set to $\Delta L_{obs} = 2.5$ cm (1.13λ at 13.5 GHz). As noticed in Fig. 8 (c) and (d), when the amplitude of the field radiated by the Tx/Rx antennas is not considered, the SAR image is degraded due to aliasing. In particular, the presence of a large scatterer (the metallic surface) results in a large replica that mixes with the replicas of the circular target.

However, when the amplitude of the field radiated by the Tx/Rx antenna is also considered in the imaging algorithm, the circular and the planar surface targets can be identified (Fig. 8 (e) and (f)). As explained in Section II.B, the use of a more directive antenna, together with the amplitude and phase compensation, results in greater mitigation of the grating lobes and, consequently, the replicas of the targets are attenuated in the SAR image. This can be noticed when comparing Fig. 8 (e) (OEWG) and Fig. 8 (f) (horn antenna): the horn antenna is more directive than the OEWG, so the aliasing has less impact in Fig. 8 (f) than in Fig. 8 (e).

IV. EXPERIMENTAL VALIDATION

In this Section, the methodology presented in Section II is validated with measurements. In the microwave imaging setups presented along this Section IV, the Tx and Rx antennas are moved along the observation domain to create a synthetic aperture. To prove that the proposed method is independent from the hardware of the microwave imaging setup, two different microwave imaging systems have been selected.

A. First validation scenario: broadband imaging setup

Measurements collected using a portable microwave imaging setup have been selected to assess the imaging method presented in this contribution. The setup, depicted in Fig. 9, is the same quasi-monostatic setup described in Section IV.C of [32].

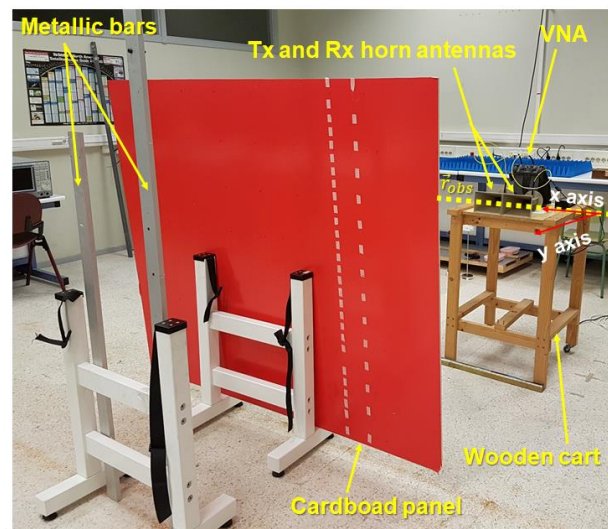


Fig. 9. Picture of the quasi-monostatic imaging setup.

The acquisition setup consisted of two horn antennas connected to a portable Vector Network Analyzer (model

TIM-22-04874R1

N9926A [41]), configured to perform measurements within the 4-6 GHz frequency band, being discretized into 41 frequency points. The transmitted power was 0 dBm. An OSL (Open-Short-Load) calibration was conducted at the connection between the horn antennas and the 75 cm-long coaxial cables connecting the antennas and the VNA ports to remove the effect of these cables in the measurements. The rest of the VNA parameters (e.g., the intermediate frequency bandwidth) were the default ones for this device. All the system was mounted on top of a wooden cart that was moved along the observation domain to create a synthetic aperture. In this example, the length of the synthetic aperture was $L_{\text{obs}} = 75$ cm, and the sampling rate $\Delta L_{\text{obs}} = 2.5$ cm (0.42λ at $f_c = 5$ GHz).

The field radiated by the horn antennas has been calculated using an analytical model of the horn antenna aperture fields [42]. This analytical model requires the following data as inputs: the size of the horn antenna aperture ($24 \text{ cm} \times 17.5 \text{ cm}$), the size of the waveguide feeding the horn antenna ($8.3 \text{ cm} \times 4.7 \text{ cm}$), and the perpendicular distance from the waveguide opening to the aperture plane of the horn antenna (25 cm).

The targets placed in the imaging domain, depicted in Fig. 9, are a cardboard panel located $R_{\text{cardboard}} = 150$ cm away from the observation domain; and two metallic bars, placed $R_{\text{bars}} = 225$ cm away from the observation domain.

SAR images plotted in Fig. 10 (a) and Fig. 10 (b) have been retrieved using the imaging algorithms based on the modified DAS that considers the phase of the field radiated by the horn antennas from (2), and the modified DAS that considers also the amplitude of the field radiated by the horn antennas as in (8), respectively. The main difference between these images is related to the reflectivity level of the cardboard panel, which is 5 dB higher when the amplitude and phase of the field radiated by the Tx and Rx horn antennas is considered.

Next, the sampling rate of the observation domain was decreased to $\Delta L_{\text{obs}} = 7.5$ cm (1.25λ at $f_c = 5$ GHz). In Fig. 10 (c), the replicas of the cardboard due to the aliasing are centered at $x = -50$ cm and $x = 75$ cm, that is, approximately ± 62.5 cm from the center of the true target. This distance is in agreement with the one predicted with (4):

$$d_{GL, \text{cardboard}} = \frac{\lambda R}{2 \Delta L_{\text{obs}}} = \frac{6 \text{ cm} \times 150 \text{ cm}}{2 \times 7.5 \text{ cm}} = 60 \text{ cm} \quad (10)$$

If $\Delta L_{\text{obs}} = 10$ cm (1.67λ at $f_c = 5$ GHz), the replicas of the cardboard panel cannot be distinguished from the true image of the target (in this case, $d_{GL, \text{cardboard}} = 45$ cm), as observed in Fig. 10 (e).

These aliasing effects are mitigated when the amplitude and phase of the field radiated by the horn antenna is considered. In this case, the two metallic bars and the cardboard panel can be still identified, not only for $\Delta L_{\text{obs}} = 7.5$ cm (Fig. 10 (d)), but also for $\Delta L_{\text{obs}} = 10$ cm (Fig. 10 (f)).

The proposed methodology has an impact in the measurement time as fewer measurements are required when the spacing between samples is widened. In this example, the use of a sampling step of 1.67λ (Fig. 10 (f)) enables to estimate a speed-up of 3.9 times with respect to the case where the

observation domain is sampled every 0.42λ (Fig. 10 (b)), as the number of measurement points is 3.9 times less ($N = 8$ in the former case, and $N = 31$ in the latter).

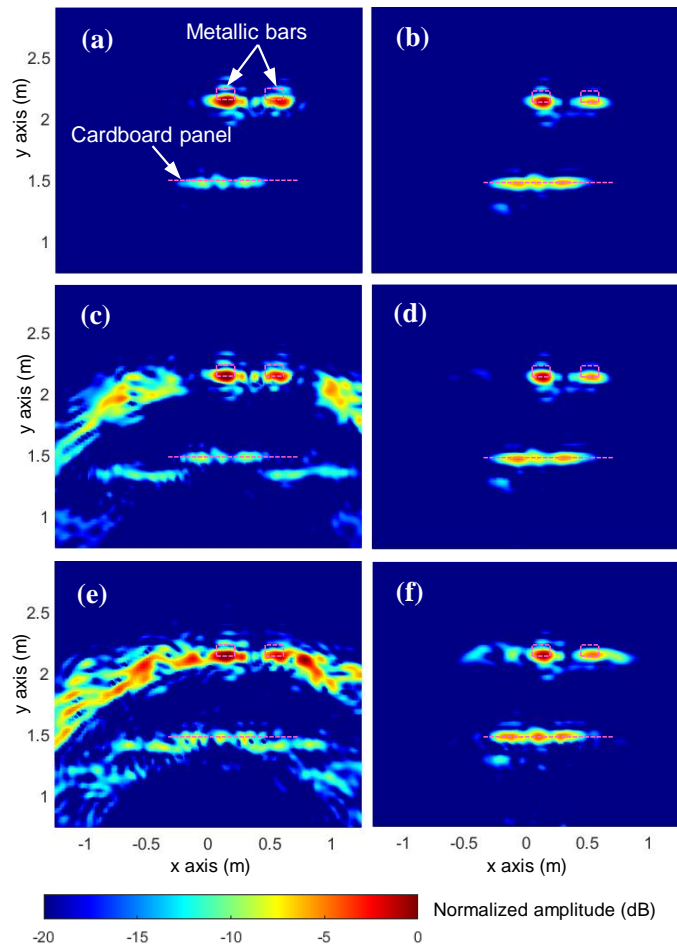


Fig. 10. Imaging results for the scenario depicted in Fig. 9. (a),(b) Observation domain sampled with $\Delta L_{\text{obs}} = 2.5$ cm (0.42λ), $N = 31$ points. (c),(d) Subsampled observation domain, $\Delta L_{\text{obs}} = 7.5$ cm (1.25λ), $N = 11$ points. (e),(f) Subsampled observation domain, $\Delta L_{\text{obs}} = 10$ cm (1.67λ), $N = 8$ points. Left column: reflectivity calculated using the phase of the field radiated by the Tx and Rx horn antennas. Right column: reflectivity calculated using the complex field radiated by the Tx and Rx horn antennas.

B. Second validation scenario: monochromatic imaging setup

The method presented in this contribution has been validated with 2D cross-range measurements collected using the measurement setup described in Section IV of [43] at a single frequency $f = 15$ GHz. This setup was devoted to validating a phaseless microwave imaging system where the phase of the measured scattered field was recovered by means of indirect holography [43]. Thus, a radiofrequency signal generator [44] and a power detector [45] were used instead of a VNA.

A scheme and a picture of the phaseless quasi-monostatic microwave imaging setup are shown in Fig. 11 (a) and (b), respectively. A directional coupler was required to obtain a reference signal whose amplitude was adjusted by means of a variable attenuator [46] before combining it with the signal coming from the Rx antenna. By means of the processing method described in [43] the phase of the field scattered by the

TIM-22-04874R1

target under test was recovered for each measurement position. Two ultrawideband amplifiers [47] were included in the measurement setup to ensure sufficient dynamic range.

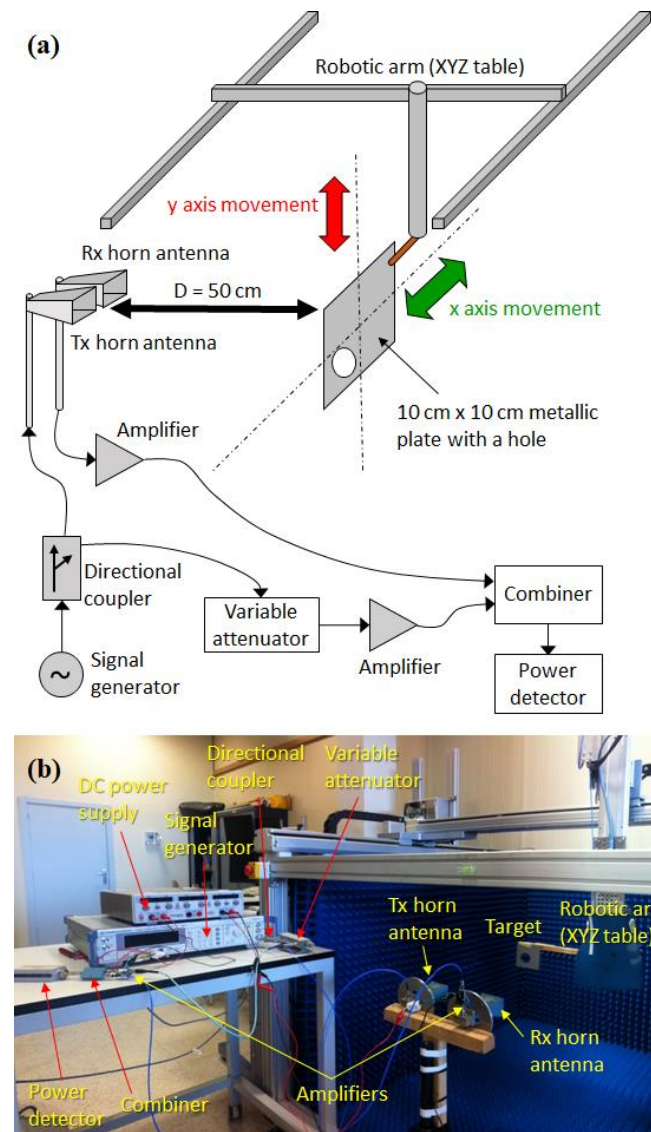


Fig. 11. (a) Scheme and (b) picture of the phaseless quasi-monostatic microwave imaging setup of Section IV.B.

The target under test, a 10 cm × 10 cm aluminum square plate with a 4 cm diameter hole in it, was mounted on a robotic arm so the target is moved instead of the Tx and Rx antennas [48].

The size of the 2D observation domain, placed $R = 50$ cm away from the metallic target, was $L_{\text{obs}} \times L_{\text{obs}} = 40$ cm × 40 cm. Both the Tx and Rx antennas were Standard Gain Horn (SGH) antennas (model SGH 639) [50], connected as shown in Fig. 11.

The SGH antennas were identical, so only one of them was characterized in a planar range (the same robotic arm as for the imaging system was used to conduct the measurement of the SGH [43]). From the measurement of the near field radiated by the SGH, the fields on the aperture plane of the SGH were recovered using the method described in [49]. Then, the aperture fields were used to compute the field radiated by the Tx and Rx SGH antennas in the imaging domain.

In this example, the reflectivity was recovered in a 40 cm × 40 cm plane placed at the same distance from the observation domain as the metallic plate ($R = 50$ cm). Imaging results for different sampling rates of the observation domain are depicted in Fig. 12, where the imaging techniques described in this contribution are also compared. Fig. 12 (a)-(c) correspond to $\Delta L_{\text{obs}} = 1$ cm (0.5λ at $f_c = 15$ GHz), thus resulting in $N = 1681$ measurement points. The DAS with the far-field approach provides an image of the target (Fig. 12 (a)) slightly sharper than the modified versions of DAS that make use of the field radiated by the SGH (Fig. 12 (b) and (c)).

Aliasing effects can be observed when the spacing between samples is increased: in the results depicted in Fig. 12 (d),(e) ($\Delta L_{\text{obs}} = 3$ cm = 1.5λ) and in Fig. 12 (g) and (h) ($\Delta L_{\text{obs}} = 4$ cm = 2λ), the replicas of the metallic plate appear every 16.7 cm and every 12.5 cm, respectively, in agreement with the theoretical positions calculated with (4):

$$d_{GL} = \frac{\lambda R}{2 \Delta L_{\text{obs}}} = \frac{2 \text{ cm} \times 50 \text{ cm}}{2 \times 3 \text{ cm}} = 16.7 \text{ cm} \quad (11)$$

$$d_{GL} = \frac{\lambda R}{2 \Delta L_{\text{obs}}} = \frac{2 \text{ cm} \times 50 \text{ cm}}{2 \times 4 \text{ cm}} = 12.5 \text{ cm} \quad (12)$$

When the amplitude and phase of the radiation pattern of the SGH are considered (Fig. 12 (f) and Fig. 12 (i)), the replicas of the imaged target are attenuated. Even when the observation domain is sampled every $\Delta L_{\text{obs}} = 2 \lambda$, the maximum reflectivity level of the replicas is 10 dB below the reflectivity level of the imaged target (Fig. 12 (i)). And for $\Delta L_{\text{obs}} = 1.5 \lambda$, the replicas are barely observed (Fig. 12 (f)). Note that, in the case of this 2D microwave imaging setup, the use of a sampling rate of $\Delta L_{\text{obs}} = 1.5 \lambda$ allows decreasing the required number of samples from $N = 1681$ points ($\Delta L_{\text{obs}} = 0.5 \lambda$) to $N = 196$ points.

C. Impact of the accuracy of the Tx/Rx antenna characterization in the SAR images

An accurate characterization of the Tx and Rx antennas is fundamental for precise imaging of the targets. In the case of horn or OEWG antennas, analytical models can model the field radiated by these antennas with an accuracy comparable to the one achieved with measurements.

To assess this, imaging results based on an analytical model [42] constructed from the physical dimensions of the SGH [42],[50], and considering an equivalent electromagnetic model of the SGH antenna (that is, using the aperture fields recovered from near field measurements of the SGH [49]), are compared in Fig. 13. The first row of images corresponds to the equivalent currents model whereas the second row corresponds to the analytical model. In both cases, the first column corresponds to the DAS with phase correction whereas the second column corresponds to the DAS with amplitude and phase correction. The analytical model provides sharper images (Fig. 13 (d)) than the electromagnetic equivalent model (Fig. 13 (b)), although at the expense of worse mitigation of the replicas of the target.

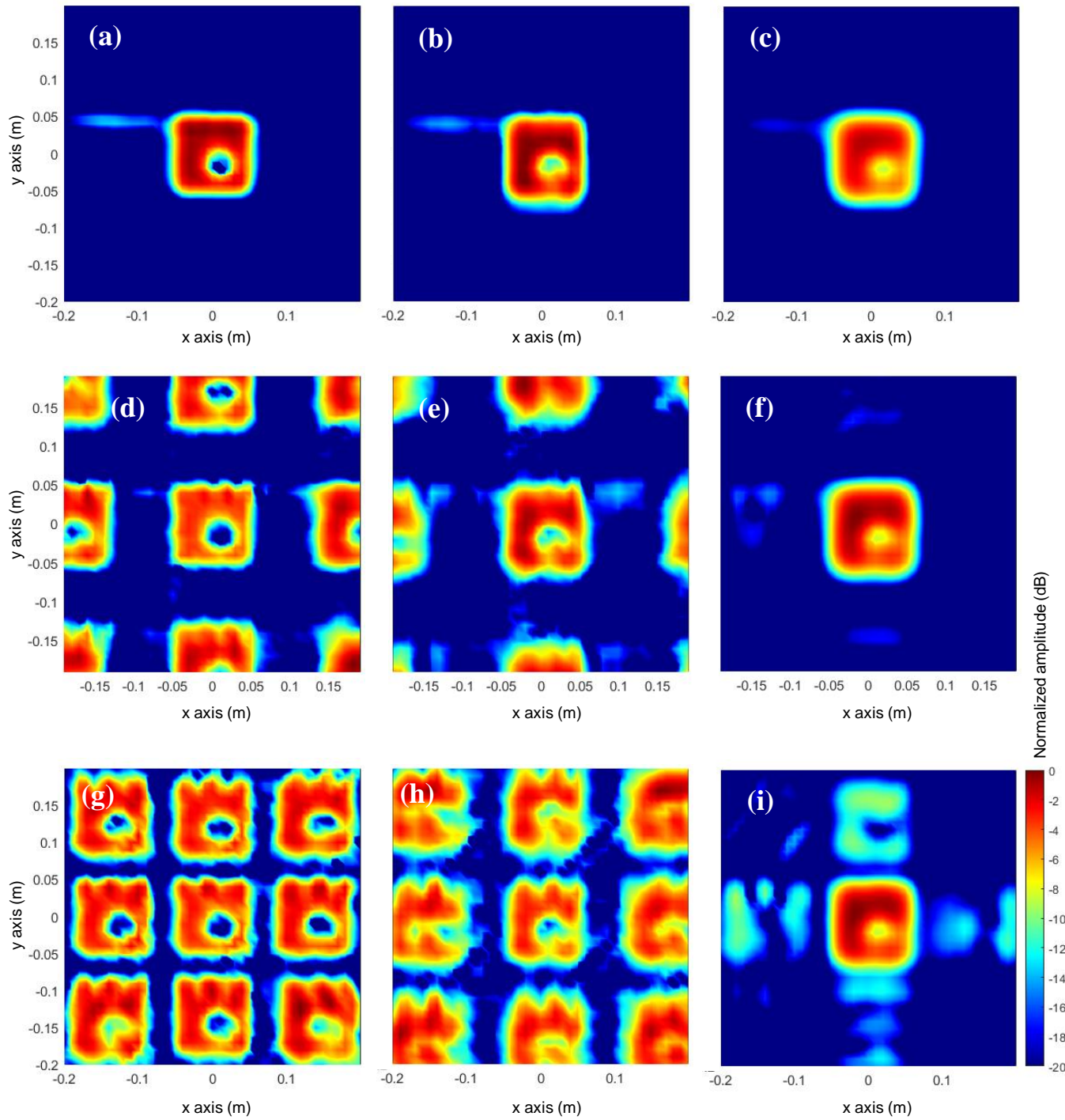


Fig. 12. Imaging results of a flat metallic plate with a hole. Tx and Rx antennas are Standard Gain Horn (SGH) antennas. (a)-(c) $\Delta L_{obs} = 1$ cm (0.5λ), (d)-(f) $\Delta L_{obs} = 3$ cm (1.5λ), (g)-(i) $\Delta L_{obs} = 4$ cm (2λ). Left column: reflectivity calculated using the far field approach. Center column: reflectivity calculated using the phase of the field radiated by the SGH. Right column: reflectivity calculated using the complex field radiated by the SGH.

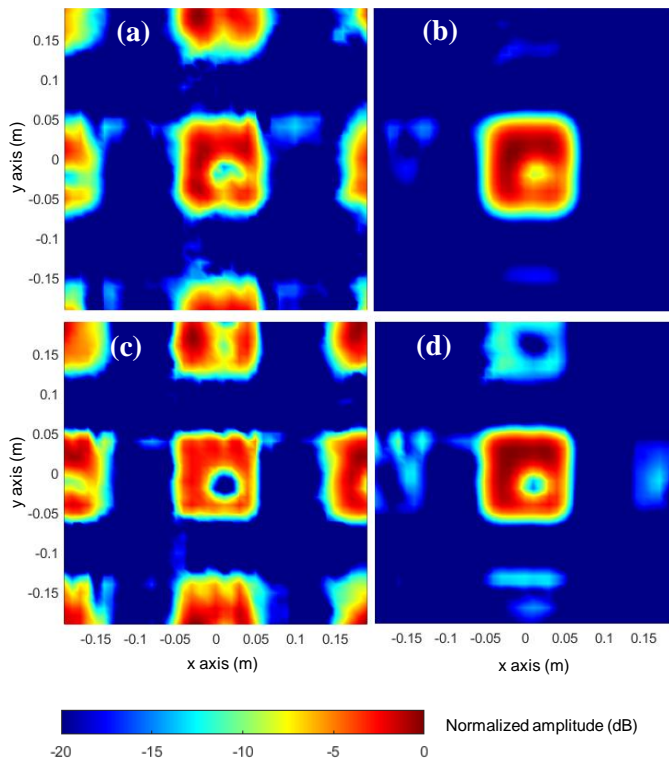


Fig. 13. Imaging results. Observation domain sampled with $\Delta L_{obs} = 3$ cm (1.5λ), $N = 196$ points. (a),(b) Reflectivity calculated using an equivalent currents model of the SGH antennas. (c),(d) Reflectivity calculated using an analytical model of the SGH antennas. (a),(c) Reflectivity calculated using the phase of the field radiated by the Tx and Rx horn antennas. (b),(d) Reflectivity calculated using the complex field radiated by the Tx and Rx horn antennas.

Thus, the degree of accuracy in the modelling of the Tx and Rx antennas and, consequently, the field radiated by these antennas within the imaging domain does have an impact in the recovered SAR images. This issue is analyzed in Fig. 14, where results for phase compensation are shown in the first column (Fig. 14 (a) and (c)), and results for phase and amplitude correction are depicted in the second column (Fig. 14 (b) and (d)). Two analytical models are considered for each imaging algorithm: the first one makes use of the exact dimensions of the SGH (first row, i.e., Fig. 14 (a) and (b)) whereas the other one is implemented from incorrect dimensions of the SGH (second row, i.e., Fig. 14 (c) and (d)). In particular, the aperture size of the SGH is doubled, and the perpendicular distance from the waveguide opening to the aperture is enlarged by a factor of 4.5. Results depicted in Fig. 14 (c) and (d) confirm that, when the incorrect SGH antenna model is used, the target is not properly imaged. This distortion is even more noticeable when only the phase of the field radiated by the Tx and Rx antennas is considered (Fig. 14 (c)).

V. CONCLUSIONS

This contribution has presented a methodology that enables the use of subsampled SAR apertures while minimizing the impact of the aliasing effects. The proposed method is based on the DAS backpropagation algorithm, modifying it to introduce the field radiated by the Tx and Rx antennas of the imaging

system. As confirmed by the simulation and measurement-based examples presented in this contribution, the directional properties of these antennas result in the attenuation of the replicas of the imaged targets.

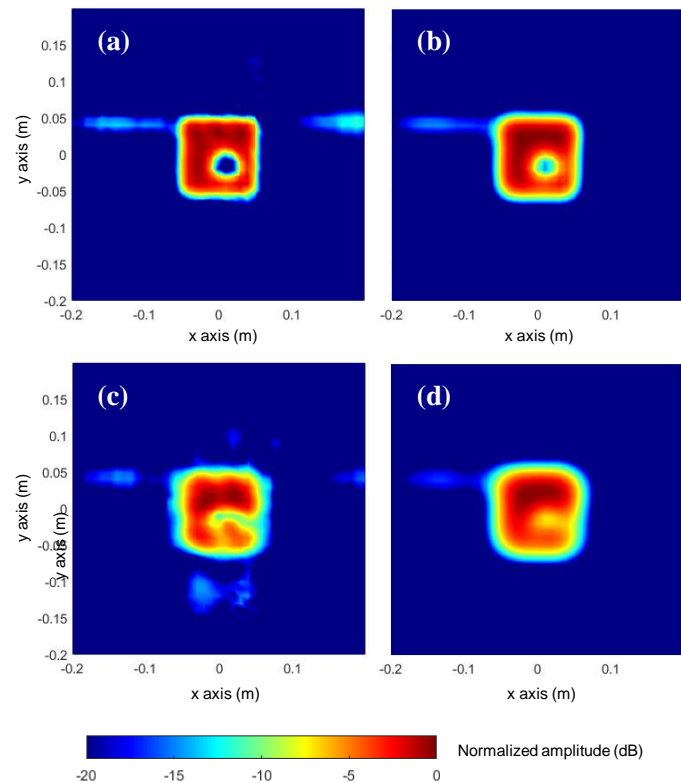


Fig. 14. Imaging results. Observation domain sampled with $\Delta L_{obs} = 2$ cm (1λ), $N = 441$ points. (a),(b) Reflectivity calculated using the correct analytical model of the SGH antennas. (c),(d) Reflectivity calculated using an incorrect analytical model of the SGH antennas. (a),(c). Reflectivity calculated using the phase of the field radiated by the Tx and Rx SGH antennas. (b),(d). Reflectivity calculated using the complex field radiated by the Tx and Rx SGH antennas.

Concerning the subsampling rate achieved with the proposed technique, Table II summarizes the results for the examples presented in this contribution. In all the cases, at least 1λ sampling rate is achieved while keeping the quality of the recovered SAR images similar to the ones retrieved when the Nyquist sampling rate is fulfilled. The achieved subsampling rate allows, at least, duplicating the scanning speed of the SAR microwave imaging for a linear scan or quadruplicating it for a planar scan.

With respect to other microwave imaging techniques for subsampled apertures, the results obtained with the methodology presented in this contribution exhibit subsampling rates within the same range as the ones obtained with other methods (see Table I of Section I.C).

The proposed method is suitable for different microwave imaging architectures (like the two ones presented in Section IV). Thus, it could be introduced, for example, in SAR-based systems for remote sensing, nondestructive inspection architectures based on microwave imaging, etc.

TABLE II
SUMMARY OF THE SUBSAMPLED SAR IMAGING EXAMPLES
PRESENTED IN THIS CONTRIBUTION.

Section	Target	Frequen- cy band	L_{obs}	R	Achieved subsampling ¹
Section III.A	Circular scatterer.	12-14 GHz	10 cm (4.3λ at f_c)	75 cm (32.5λ at f_c)	$\Delta L_{\text{obs}} = 2.5$ cm (1.08λ)
Section III.B	Circular scatterer in front of a 1 m wide metallic panel.	12-15 GHz	55 cm (24.8λ at f_c)	80 cm (36λ at f_c)	$\Delta L_{\text{obs}} = 2.5$ cm (1.13λ)
Section IV.A	Two metallic bars behind a 75 cm wide cardboard panel.	4-6 GHz	75 cm (12.5λ at f_c)	150 cm and 225 cm (25λ and 37.5λ at f_c)	$\Delta L_{\text{obs}} = 10$ cm (1.67λ)
Section IV.B	Flat metallic plate (10 cm \times 10 cm) with a hole.	15 GHz	20 cm \times 20 cm ($10 \lambda \times 10 \lambda$ at f_c)	50 cm (25λ at f_c)	$\Delta L_{\text{obs}} = 3$ cm (1.5λ)

¹ In all the examples, maximum subsampling is achieved with a horn Tx/Rx antenna.

ANNEX I

This Annex describes the calculation of the field radiated by the Tx/Rx antenna of the microwave imaging system. The methodology is particularized for directive antennas, as they allow achieving the subsampling rates with the proposed imaging technique.

Directive antennas can be characterized by the distribution of the electric field on the antenna aperture, $\vec{E}_{ap}(\vec{r}_{ap})$ [51]. By means of the application of the electromagnetic Equivalence Principle [51],[52], an equivalent magnetic currents distribution on the aperture plane, $\vec{M}_{eq}(\vec{r}_{ap})$, is given by (13):

$$\vec{M}_{eq}(\vec{r}_{ap}) = -2\hat{n} \times \vec{E}_{ap}(\vec{r}_{ap}) \quad (13)$$

Next, the electric field radiated in the region of the space in front of the aperture of the Tx/Rx antenna (which includes the imaging domain, \vec{r}') is calculated by means of the integral equation relating the equivalent magnetic currents $\vec{M}_{eq}(\vec{r}_{ap})$ and the radiated electric field (14):

$$\vec{E}_{rad}(\vec{r}') = -\frac{1}{4\pi} \nabla \times \int_{S_{ap}} \vec{M}_{eq}(\vec{r}_{ap}) \frac{e^{-jk_0|\vec{r}'-\vec{r}_{ap}|}}{|\vec{r}'-\vec{r}_{ap}|} dS_{ap} \quad (14)$$

Note that if a point source was considered in (14), this equation could be simplified, and the field in the imaging domain would be given by $e^{-jk_0|\vec{r}'-\vec{r}_{ap}|}/|\vec{r}'-\vec{r}_{ap}|$, whose amplitude change is usually neglected and, therefore, it corresponds to the far field term of the radiated field.

The generalized formulation based on the use of equivalent electric and magnetic currents to characterize the Tx/Rx antenna is provided in Section III.B of [32].

REFERENCES

- [1] A. Rosenqvist, C. E. Jones, E. Rignot, M. Simons, P. Siqueira and T. Tadono, "A Review of SAR Observation Requirements for Global and Targeted Science Applications," *2021 IEEE International Geoscience and Remote Sensing Symposium IGARSS*, 2021, pp. 1745-1748, doi: 10.1109/IGARSS47720.2021.9553966.
- [2] H. McNairn, L. D. Robertson, D. Tsan, X. Jiao and A. Davidson, "Multi-Frequency SAR to Monitor Agriculture in the Americas," *2021 IEEE International Geoscience and Remote Sensing Symposium IGARSS*, 2021, pp. 5914-5916, doi: 10.1109/IGARSS47720.2021.9555034.
- [3] F. Xue, X. Lv, F. Dou and Y. Yun, "A Review of Time-Series Interferometric SAR Techniques: A Tutorial for Surface Deformation Analysis," in *IEEE Geoscience and Remote Sensing Magazine*, vol. 8, no. 1, pp. 22-42, March 2020, doi: 10.1109/MGRS.2019.2956165.
- [4] C. Liu and R. Zoughi, "Adaptive Synthetic Aperture Radar (SAR) Imaging for Optimal Cross-Range Resolution and Image Quality in NDE Applications," *IEEE Transactions on Instrumentation and Measurement*, vol. 70, pp. 1-7, 2021, Art no. 8005107, doi: 10.1109/TIM.2021.3118080.
- [5] C. Noviello *et al.*, "Monitoring Buildings at Landslide Risk With SAR: A Methodology Based on the Use of Multipass Interferometric Data," in *IEEE Geoscience and Remote Sensing Magazine*, vol. 8, no. 1, pp. 91-119, March 2020, doi: 10.1109/MGRS.2019.2963140.
- [6] A. Moreira, P. Prats-Iraola, M. Younis, G. Krieger, I. Hajnsek and K. P. Papathanassiou, "A tutorial on synthetic aperture radar," in *IEEE Geoscience and Remote Sensing Magazine*, vol. 1, no. 1, pp. 6-43, March 2013, doi: 10.1109/MGRS.2013.2248301.
- [7] J. Laviada, Y. Álvarez-López, A. Arboleya-Arboleya, C. García-González and F. Las-Heras, "Interferometric Technique With Nonredundant Sampling for Phaseless Inverse Scattering," *IEEE Transactions on Antennas and Propagation*, vol. 62, no. 2, pp. 739-746, Feb. 2014, doi: 10.1109/TAP.2013.2291238.
- [8] X. Zhuge and A. G. Yarovoy, "A Sparse Aperture MIMO-SAR-Based UWB Imaging System for Concealed Weapon Detection," in *IEEE Transactions on Geoscience and Remote Sensing*, vol. 49, no. 1, pp. 509-518, Jan. 2011, doi: 10.1109/TGRS.2010.2053038.
- [9] S. S. Ahmed, A. Schiess and L. -P. Schmidt, "Near field mm-wave imaging with multistatic sparse 2D-arrays," *2009 European Radar Conference (EuRAD)*, 2009, pp. 180-183.
- [10] S. S. Ahmed, A. Schiessl and L. Schmidt, "A Novel Fully Electronic Active Real-Time Imager Based on a Planar Multistatic Sparse Array," in *IEEE Transactions on Microwave Theory and Techniques*, vol. 59, no. 12, pp. 3567-3576, Dec. 2011, doi: 10.1109/TMTT.2011.2172812.
- [11] T. J. Brockett and Y. Rahmat-Samii, "Subarray Design Diagnostics for the Suppression of Undesirable Grating Lobes," in *IEEE Transactions on Antennas and Propagation*, vol. 60, no. 3, pp. 1373-1380, March 2012, doi: 10.1109/TAP.2011.2180333.
- [12] Z. Iqbal and M. Pour, "Grating Lobe Reduction in Scanning Phased Array Antennas With Large Element Spacing," in *IEEE Transactions on Antennas and Propagation*, vol. 66, no. 12, pp. 6965-6974, Dec. 2018, doi: 10.1109/TAP.2018.2874717.
- [13] M. Burns, S. Laxpati and J. Shelton, "A comparative study of linear array synthesis technique using a personal computer," in *IEEE Transactions on Antennas and Propagation*, vol. 32, no. 8, pp. 884-887, August 1984, doi: 10.1109/TAP.1984.1143426.
- [14] Y. Álvarez, Y. Rodríguez-Vaqueiro, B. Gonzalez-Valdes, J. Á. Martínez-Lorenzo, F. Las-Heras and C. M. Rappaport, "Phase Error Compensation in Imaging Systems Using Compressed Sensing Techniques," in *IEEE Antennas and Wireless Propagation Letters*, vol. 12, pp. 1574-1577, 2013, doi: 10.1109/LAWP.2013.2293314.
- [15] Y. Rodríguez-Vaqueiro, Y. Álvarez López, B. González-Valdes, J. Á. Martínez, F. Las-Heras and C. M. Rappaport, "On the Use of Compressed Sensing Techniques for Improving Multistatic Millimeter-Wave Portal-Based Personnel Screening," *IEEE Transactions on Antennas and Propagation*, vol. 62, no. 1, pp. 494-499, Jan. 2014. doi: 10.1109/TAP.2013.2287902.
- [16] L. Huang and Y. Lu, "Microwave imaging with random sparse array and compressed sensing for target detection," *2015 IEEE International Conference on Computational Electromagnetics*, 2015, pp. 124-125, doi: 10.1109/COMPEM.2015.7052578.
- [17] Y. Álvarez, M. García-Fernández, L. Poli, C. García-González, P. Rocca, F. las-Heras and A. Massa, "Inverse Scattering for Monochromatic Phaseless Measurements," *IEEE Transactions on Instrumentation and Measurement*, vol. 66, no. 1, pp. 45-60, Jan. 2017, doi: 10.1109/TIM.2016.2615478.

TIM-22-04874R1

- [18] Ron Goodman, Walter Carrara, 10.1 - Synthetic Aperture Radar Algorithms, Editor(s): AL BOVIK, In Communications, Networking and Multimedia, Handbook of Image and Video Processing (Second Edition), Academic Press, 2005, Pages 1131-1153, ISBN 9780121197926, <https://doi.org/10.1016/B978-012119792-6/50127-3>.
- [19] S. R. DeGraaf, "SAR imaging via modern 2-D spectral estimation methods," in *IEEE Transactions on Image Processing*, vol. 7, no. 5, pp. 729-761, May 1998, doi: 10.1109/83.668029.
- [20] Hong Wen and Mao Shiyi, "Fourier reconstruction in spotlight mode SAR imaging," *Proceedings of International Radar Conference*, 1996, pp. 338-341, doi: 10.1109/ICR.1996.574456.
- [21] J. Zhang and D. Wang, "A Novel Fast Imaging Method for Microwave Array," *2021 International Conference on Microwave and Millimeter Wave Technology (ICMMT)*, 2021, pp. 1-3, doi: 10.1109/ICMMT52847.2021.9618311.
- [22] J. Wang, P. Aubry and A. Yarovoy, "3-D Short-Range Imaging With Irregular MIMO Arrays Using NUFFT-Based Range Migration Algorithm," in *IEEE Transactions on Geoscience and Remote Sensing*, vol. 58, no. 7, pp. 4730-4742, July 2020, doi: 10.1109/TGRS.2020.2966368.
- [23] M. I. Duersch, "Backprojection for Synthetic Aperture Radar". Ph.D. Dissertation. Brigham Young University. 13-06-2013. Online. Available at: <https://scholarsarchive.byu.edu/cgi/viewcontent.cgi?article=5059&context=etd> [last accessed: 05-20-2022].
- [24] V. Perrot, M. Polichetti, F. Varray and Damien Garcia, "So you think you can DAS? A viewpoint on delay-and-sum beamforming," *Ultrasonics*, Volume 111, 2021, 106309, doi: 10.1016/j.ultras.2020.106309.
- [25] Y. Yang, Z. Chu, L. Shen and Z. Xu, "Functional delay and sum beamforming for three-dimensional acoustic source identification with solid spherical arrays," *Journal of Sound and Vibration*, Vol. 373, pp. 340-359, 2016. doi: 10.1016/j.jsv.2016.03.024
- [26] P. Mojabi, M. Ostadrahimi, L. Shafai and J. LoVetri, "Microwave Etomography techniques and algorithms: A review," *2012 15 International Symposium on Antenna Technology and Applied Electromagnetics*, 2012, pp. 1-4, doi: 10.1109/ANTEM.2012.6262367.
- [27] R. Persico, F. Soldovieri and G. Leone, "A Microwave Tomographic Imaging Approach for Multibistatic Configuration: The Choice of the Frequency Step," *IEEE Transactions on Instrumentation and Measurement*, vol. 55, no. 6, pp. 1926-1934, Dec. 2006, doi: 10.1109/TIM.2006.884346.
- [28] B. Wu, Y. Gao, J. Laviada, M. T. Ghasr and R. Zoughi, "Time-Reversal SAR Imaging for Nondestructive Testing of Circular and Cylindrical Multilayered Dielectric Structures," *IEEE Transactions on Instrumentation and Measurement*, vol. 69, no. 5, pp. 2057-2066, May 2020, doi: 10.1109/TIM.2019.2918371.
- [29] K. Aberman and Y. C. Eldar, "Sub-Nyquist SAR via Fourier Domain Range-Doppler Processing," *IEEE Transactions on Geoscience and Remote Sensing*, vol. 55, no. 11, pp. 6228-6244, Nov. 2017. doi: 10.1109/TGRS.2017.2723620.
- [30] [36] Y. Álvarez, Y. Rodríguez-Vaqueiro, B. González-Valdés, F. Las-Heras, A. García-Pino, "Fourier-based imaging for subsampled multistatic arrays," *IEEE Transactions on Antennas and Propagation*, Vol. 64, No. 6, pp. 2557-2562, June 2016. doi: 10.1109/TAP.2016.2550035.
- [31] Z. Iqbal and M. Pour, "Grating Lobe Mitigation in Wide and Near Horizon Scanning Linear Arrays with One-Wavelength Element Spacing," *2021 IEEE 19th International Symposium on Antenna Technology and Applied Electromagnetics (ANTEM)*, 2021, pp. 1-2, doi: 10.1109/ANTEM51107.2021.9518636.
- [32] Y. Álvarez and F. Las-Heras, "On the use of an Equivalent Currents-based Technique to improve Electromagnetic Imaging," *IEEE Transactions on Instrumentation and Measurement*, vol. 71, pp. 1-13, 2022, art. no. 8004113, doi: 10.1109/TIM.2022.3181926.
- [33] S. Sayed Ahmed, "Electronic Microwave Imaging with Planar Multistatic Arrays". Ph.D. Dissertation. Faculty of Engineering, Universität Erlangen-Nürnberg. April 2013. Online: https://opus4.kobv.de/opus4-fau/files/6500/Dissertation_SherifAhmed.pdf [last accessed 25-6-22].
- [34] C. Liu, M. T. A. Qaseer and R. Zoughi, "Influence of Antenna Pattern on Synthetic Aperture Radar Resolution for NDE Applications," *IEEE Transactions on Instrumentation and Measurement*, vol. 70, pp. 1-11, 2021, Art no. 8000911, doi: 10.1109/TIM.2020.3026122.
- [35] B. Mamandipoor, M. Fallahpour, G. Malysa, K. Noujeim, U. Madhow and A. Arbabian, "Spatial-domain technique to overcome grating lobes in sparse monostatic mm-wave imaging systems," *2016 IEEE MTT-S International Microwave Symposium (IMS)*, 2016, San Francisco, USA; 22-27 May 2016, pp. 1-4. doi: 10.1109/MWSYM.2016.7540151.
- [36] B. Mamandipoor, M. Fallahpour, A. Arbabian, and U. Madhowa, "Millimeter wave imaging using sparse arrays", *Signal Processing*, Vol. 164, November 2019, pp. 301-312. doi: 10.1016/j.sigpro.2019.06.016.
- [37] M. E. Yanik, and M- Torlak, "Near-Field MIMO-SAR Millimeter-Wave Imaging With Sparsely Sampled Aperture Data," *IEEE Access*, Vol. 7, pp. 31801-31819, 2019. doi: 10.1109/ACCESS.2019.2902859.
- [38] M. Kazemi, Z. Kavehvash and M. Shabany, "K-Space Analysis of Aliasing in Millimeter-Wave Imaging Systems," in *IEEE Transactions on Microwave Theory and Techniques*, vol. 69, no. 3, pp. 1965-1973, March 2021, doi: 10.1109/TMTT.2021.3053238.
- [39] M. Lort, A. Aguasca, C. López-Martínez and T. M. Marín, "Initial Evaluation of SAR Capabilities in UAV Multicopter Platforms," in *IEEE Journal of Selected Topics in Applied Earth Observations and Remote Sensing*, vol. 11, no. 1, pp. 127-140, Jan. 2018, doi: 10.1109/JSTARS.2017.2752418.
- [40] P. Brotzer, E. M. Domínguez and D. Henke, "Prototype of a Small, Agile, Drone-Based SAR System and Preliminary Focusing Results," *2021 IEEE International Geoscience and Remote Sensing Symposium IGARSS*, 2021, pp. 639-642, doi: 10.1109/IGARSS47720.2021.9553291.
- [41] N9926 FieldFox Handheld Microwave Vector Network Analyzer, from Keysight. Online: <https://www.keysight.com/us/en/product/N9926A/fieldfox-a-handheld-microwave-vector-network-analyzer-14-ghz.html> [last accessed: 16-09-2022].
- [42] S. J. Orfanidis. "Electromagnetic Waves and Antennas". Chapter 21, "Aperture Antennas". ECE Department. Rutgers University. Piscataway, USA. 2016. Online. Available at: <https://www.ece.rutgers.edu/~orfanidi/ewa/ch21.pdf> [last accessed: 05-20-2022].
- [43] J. Laviada, Y. Álvarez-López, A. Arboleya-Arboleya, C. García-González and F. Las-Heras, "Microwave phaseless inverse scattering setup based on indirect holography," 2013 7th European Conference on Antennas and Propagation (EuCAP), 2013, Gothenburg, Sweden, 8-12 April 2013. pp. 4057-4060.
- [44] SMR40 signal generator from Rohde & Schwarz. Online: <https://bit.ly/3DOagGn> [last accessed 17-09-2022].
- [45] E4416A EPM-P Single-Channel Power Meter from Keysight. Online: <https://www.keysight.com/us/en/product/E4416A/epm-p-series-single-channel-power-meter.html> [last accessed 20-09-2022].
- [46] 8495B manual attenuator, 18 GHz, 11 dB, 1-dB Steps, from Keysight. Online: <https://www.keysight.com/us/en/product/8494B/manual-attenuator-18-ghz-11-db-1-db-steps.html> [last accessed 20-09-2022].
- [47] Ultrawideband amplifier A182275 from Herotek. Online: <http://www.herotek.com/datasheets/pdf/Miniature-Ultra-Wideband-RF-Amplifiers-05-40Ghz.pdf> [last accessed 17-09-2022].
- [48] A. Arboleya, Y. Álvarez and F. Las-Heras, "Millimeter and submillimeter planar measurement setup," *2013 IEEE Antennas and Propagation Society International Symposium (APSURSI)*, Orlando, USA, 7-13 July 2013, pp. 1-2, doi: 10.1109/APS.2013.6710661.
- [49] Y. Alvarez, F. Las-Heras Andres, M. R. Pino and T. K. Sarkar, "An Improved Super-Resolution Source Reconstruction Method," *IEEE Transactions on Instrumentation and Measurement*, vol. 58, no. 11, pp. 3855-3866, Nov. 2009, doi: 10.1109/TIM.2009.2020847.
- [50] Specifications of the Standard Gain Horn Antenna SGH 639, from Narda. Online. Available at: https://nscainc.com/wp-content/uploads/pdf/NARDA_640.pdf [last accessed: 05-25-2022].
- [51] Sophocles J. Orfanidis, "Electromagnetic Waves and Antennas". Chapter 18: *Radiation from Apertures*. pp. 800-843. 2016. Online. Available at: <https://www.ece.rutgers.edu/~orfanidi/ewa/ch18.pdf> [last accessed: 23-09-2022].
- [52] S. R. Rengarajan and Y. Rahmat-Samii, "The field equivalence principle: illustration of the establishment of the non-intuitive null fields," *IEEE Antennas and Propagation Magazine*, vol. 42, no. 4, pp. 122-128, Aug. 2000, doi: 10.1109/74.868058.